Chapter 6

MODEL DEVELOPMENT III

Application to ice rubble

In Chapter 5 detailed measurements were used to develop force models for structure interactions with "sand keels" analogous to first-year ridge keels. The validity of applying these force models to ice rubble-structure interaction experiments is tested in this chapter. Force data reviewed in Chapter 4 are used in this study which first considers vertical structures and later examines forces on cones.

6.1 Vertical structure interaction model

Section 5.2 describes the procurement of sand tests aimed at elucidating keel failure mechanics. A force prediction model developed for sand performed well and so it is tested in this section against laboratory results for ice rubble-structure interactions. Computed forces are compared to measured forces using regression techniques and recommendations for better modelling are given.

6.1.1 Model application procedure

The sand force model described in Section 5.2 can be extended to include the effects of cohesion (after Jumikis, 1984) and thus has been adapted for this study as follows:

$$F = \frac{1}{2}\gamma H_p^2 D_{eff} K_p + 2cH_p D_{eff}\sqrt{K_p} \qquad (73)$$

where γ is the buoyant weight of submerged rubble, H_p is rubble depth at the point of peak load, D_{eff} is effective structure width, K_p is the passive pressure coefficient and c is cohesion. Rubble buoyant weight is computed here as

$$\gamma = (\rho_w - \rho_i)(1-e)g \tag{74}$$

where ρ_w and ρ_i are water and ice densities, e is bulk porosity and g is the gravitational constant.

In Section 5.1 arguments which support the omission of surcharge effects underwater for ice rubble laboratory experiments are presented. Video observations from IMD tests show that displaced rubble sometimes accumulates in front of the structure but often appears "suspended". In the present study the hypothesis tested is that displaced rubble does not create a surcharge. Thus for data from those studies where continuous ice rubble layers were indented, H_p, is assumed to be the far field depth. Where discontinuous ridges were indented, depth is computed as a function of penetration into a "sine-shaped" keel (as described in Section 4.1) as follows:

$$H_p = H\left[\sin\frac{\pi P_{en}}{W}\right] \tag{75}$$

where H and W are the keel depth and width and P_{en} is the penetration at peak force determined using the relationship derived in the sand tests (section 5.2) as

$$\frac{P_{en}}{D} = 0.113\left[\frac{W}{D}\right]^{1.63}\left[\frac{H}{D}\right]^{-0.42} \tag{76}$$

The effective diameter of the laboratory structures is approximated by the formula

$$D_{eff} = D\left[1+\frac{3H}{2D}\right] \leq 2D \qquad (77)$$

derived in Section 5.2.

The internal friction angle and cohesion used in this study are those reported in each reference source. For comparison, values of ϕ and c estimated from the regression equations derived in Section 4.2 are also used:

$$\phi = 1.22 - 168L_i + 1.7e \quad ; \quad c = 16242L_i - 7 \qquad (78)$$

where L_i is block thickness.

The passive pressure coefficient K_p defined in Equation (61) is used here. For this study structure slope was 0° for all data sets. The dynamic ice-structure friction angle, ϕ_1, was determined from friction coefficients, $\tan(\phi_1)$, where quoted in the reference source. Coefficients were estimated for IMD studies (McKenna *et al.*, 1995a and 1995b, and McKenna, 1996) to be 0.03, Keinonen and Nyman (1978) estimated a value of 0.158 and a value of 0.13 (equivalent to the IMD cone) has been assigned where no specific information was given. The surface slope, δ, of the rubble in the path of the indenting structure was estimated by the same model used in section 5.2 for the sand tests:

$$\delta = atan\left[\frac{H}{W}\right] \qquad (79)$$

where it has been assumed that the rupture surface extends from the structure to the rear of the ridge keel at peak force. Where a continuous layer of rubble was indented a slope of 0° was assumed.

6.1.2 Measured vs computed forces

All interaction data sets from Section 4.2 for which a ϕ and c were stated (excludes Timco and Cornett, 1995 and Bruneau, 1994a "dry") have been used in this comparative study. Forces measured in these tests are plotted in Figure 6.1 against forces predicted using the above procedure. The "perfect match" (1:1) line has also been drawn. Only the data sets from Chapter 3 are plotted in Figure 6.2. Computed forces are generally conservative (higher than measured) with most data points lying to the left of the 1:1 line. The poorest matching data appear to come from Cheng and Tatinclaux (1977) and Bruneau (1994a) "wet". In Figure 6.3 and 6.4 computed values of ϕ and c (from Section 4.2) were substituted for reported values. Both Cheng and Bruneau data sets appear closer to the rest in Figure 6.3 than in Figure 6.1, suggesting that the reported failure criteria may be inappropriate. This, however, is not an entirely satisfactory explanation since other data sets move away from the best-fit line when computed values of ϕ and c are used. Most importantly the McKenna *et al.* (1995b) and McKenna (1996) data which feature prominently in this thesis are negatively affected (Figure 6.4 compared to Figure 6.2).

To test the performance of the modelling technique quantitatively, ordinary least squares fitting has been applied to the data from Figures 6.1 and 6.3. Both linear and power law fits are shown in Figures 6.5 and 6.6. Due to the significant range of force experiments the larger scale tests are weighted heavier in the linear comparison. It is readily observed

in Figure 6.5 that the linear relation for the "computed ϕ-c" forces is inferior to that for the "referenced ϕ-c" force estimates (77% to 91%). Power law fits favour the "computed ϕ-c" results by a ratio of 83% to 66%. On average, the predicted forces were 18% higher than the measured for the "referenced ϕ-c" force estimates, and 33% higher for the "computed ϕ-c" force estimates. The results for the Chapter 3 data plotted in Figures 6.2 and 6.4 feature linear $\mathbf{r}^2$ values of 89% (for the referenced ϕ-c force estimates) and 65% (for the "computed ϕ-c force estimates) respectively (Figure 6.6.

Isolating the two large-scale experiment data sets, McKenna *et al.*, (1995b) and McKenna (1996), it is possible to investigate model performance further as shown in Figure 6.7. Only predicted forces using the "referenced ϕ-c" values are considered. The plot shows that forces from the first experiment are over-predicted by a wider margin than those of the second, which practically straddle the 1:1 fit line. The goodness-of-fit linear $\mathbf{r}^2$ value is 81% as shown in the figure. With zero intercept the best fit line has slope of 0.967, suggesting almost no conservatism in the estimates overall.

Figure 6.8 shows that interaction speeds have little effect on predictions. Slow and fast experiments alike fall near the match line. Note that the higher of the two medium speeds were all from the data set McKenna *et al.* (1995b). Figure 6.9 separates the experiments based on the vertical position of the conical ice shield relative to the waterline. The cone base marks the top of the cylinder considered here. It may be argued that the cone positioned low in the water would tend to interfere more with the keel below it. This assertion is supported by all but one data point so cone position relative to keel depth may be a valid consideration for ice load modelling.

Figure 6.10 shows that block strength has little or no effect on interaction forces. Weak and strong rubble blocks alike constituted ridges which were both over and under-predicted. Two additional data points have been singled out on Figure 6.10. These represent the interaction force for the experiment with no refrozen core, and, an oblique (45°) ridge test. As can be seen in the figure neither are anomalous in the prediction of forces. In summary, the separation of McKenna *et al.* (1995b) and McKenna (1996) data sets revealed in Figure 6.7 is not explained in this study.

6.1.3 Conclusions

The force prediction technique developed for sand in Chapter 5, does offer a viable prediction model for ice ridge keel forces. The technique performs well when the surcharge observed in the sand tests is left out. The model involves utilizing an effective structure width and approximated keel shape developed earlier in the thesis. These adaptations now provide some insight into the composition of the proportionality coefficients of the regression formulas established in Chapter 4.

Many variables contribute to error in force prediction. In general, one might expect a non-bias cumulative error in the variables to result in a uniform scatter of the predicted data. But trends in the residuals from comparative studies suggest that a factor causing some bias may be involved. The over-estimation of interaction forces in the broad base data set may be partially explained by the limitations of the passive earth pressure formula. This formulation is developed from a force equilibrium on a theoretical failure wedge shape which differs slightly from that typically observed (Siemens *et al.* 1965). The equilibrium of forces used also assumes that shear resistance acts over the entire failure surface instantaneously. This roughly approximates the physics of the failure

though actual failure is more likely to be progressive, initiated at the high stress zones first. In geotechnical engineering it is recognised that in computations of embankment stability, for instance, failure over the entire slip surface is non-simultaneous (Kosar, 1996). An effective shear strength is used to avoid complex numerical methods which are required to attempt precise physical modelling.

For ice ridge keels progressive failure *is* likely so that the force equilibrium method of determining forces on the surfaces of a failure wedge becomes an approximation of the actual physics. Maattanen (1994b) points out that a progressive failure index typical for sand-steel interactions is 0.8 so that one may expect applied forces to be 20% less than those computed using classical force equilibrium methods. In this study it is shown that predicted forces are, on average, 18% higher than measured forces for the entire data set. Progressive failure may be partially responsible. There is little doubt that a similar progressive failure process influences the results of direct shear box tests. The action of shearing a bulk rubble sample by applying pressure at one or both ends of a box or ring replicates the conditions for non-simultaneous failure. A consideration of box size and mechanics becomes important if one is to determine the degree to which progressive failure is an intrinsic factor in the computed ϕ and c values.

The quality-of-fit reported in the multi-variable regression analysis in section 4.2.4 was somewhat better than that reported for the analysis above. This is not surprising since it is unusual to out-perform the best-fit formulas with analytical models developed from the same data set. The fundamental problem with regression formulas is that they provide very little guidance for extrapolation. Using an analytical model based on sound principles and validated through experimental studies provides a more sound approach

for load prediction. This study has justified the use of passive earth force modelling techniques already in the literature, and demonstrates that combined with empirical formulations for effective structure width, keel shape, and the penetration at peak force, this approach can be a potent load estimating tool for ridge keel/structure interactions.

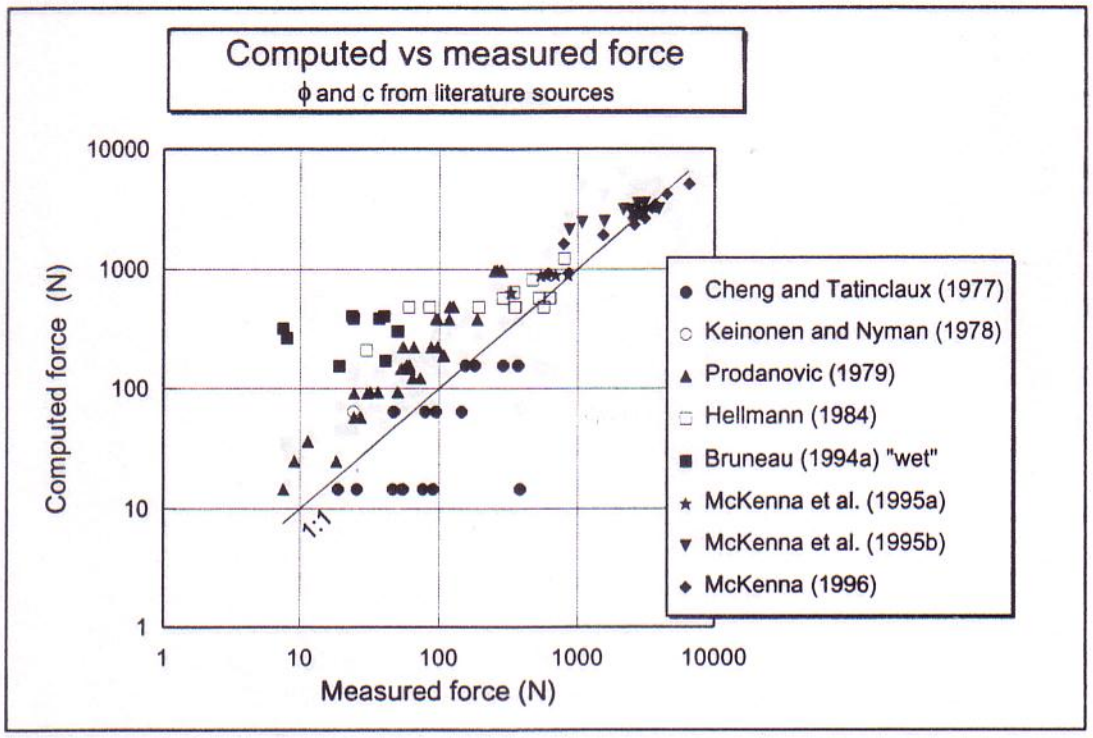

Figure 6.1 Force prediction study for "referenced ϕ-c" - by reference, base data set.

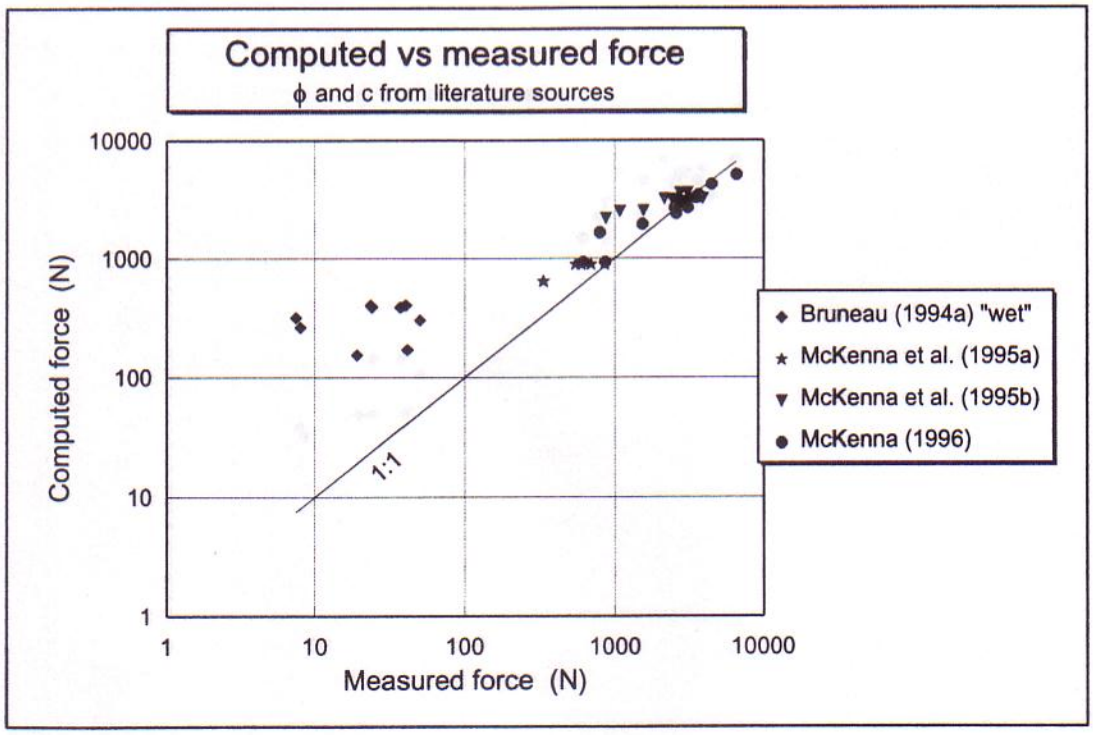

Figure 6.2 Force prediction study for "referenced ϕ-c" - Chapter 3 data.

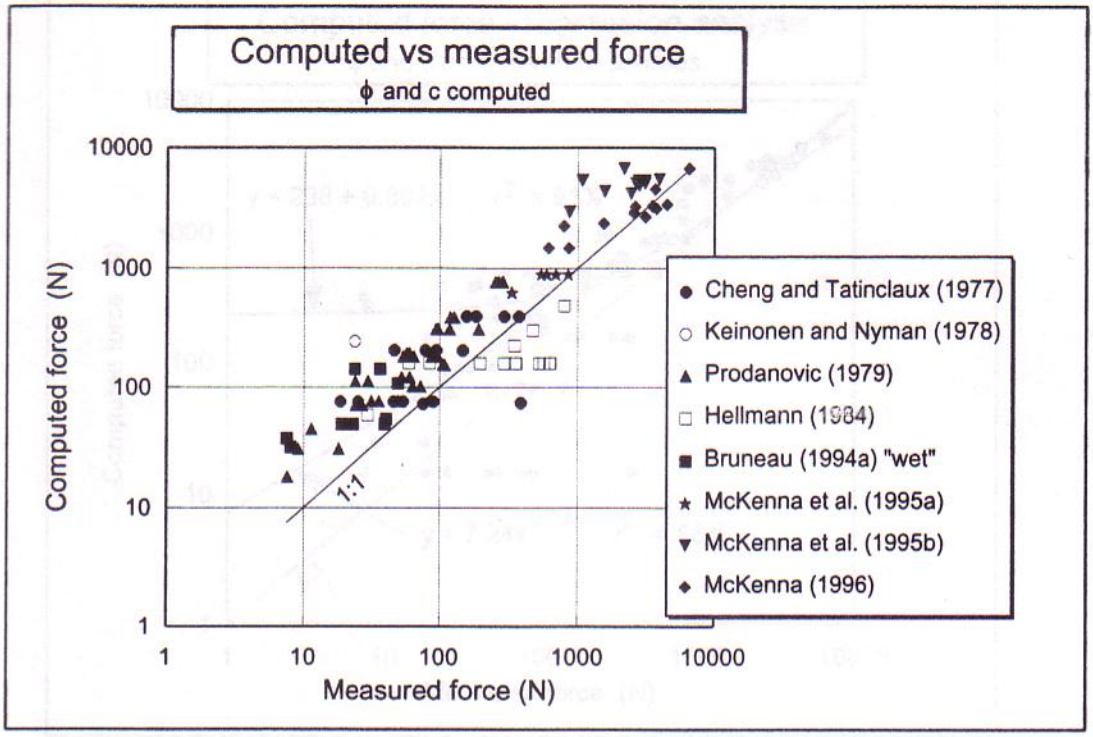

Figure 6.3 Force prediction study for "computed ϕ-c" - by reference, base data set.

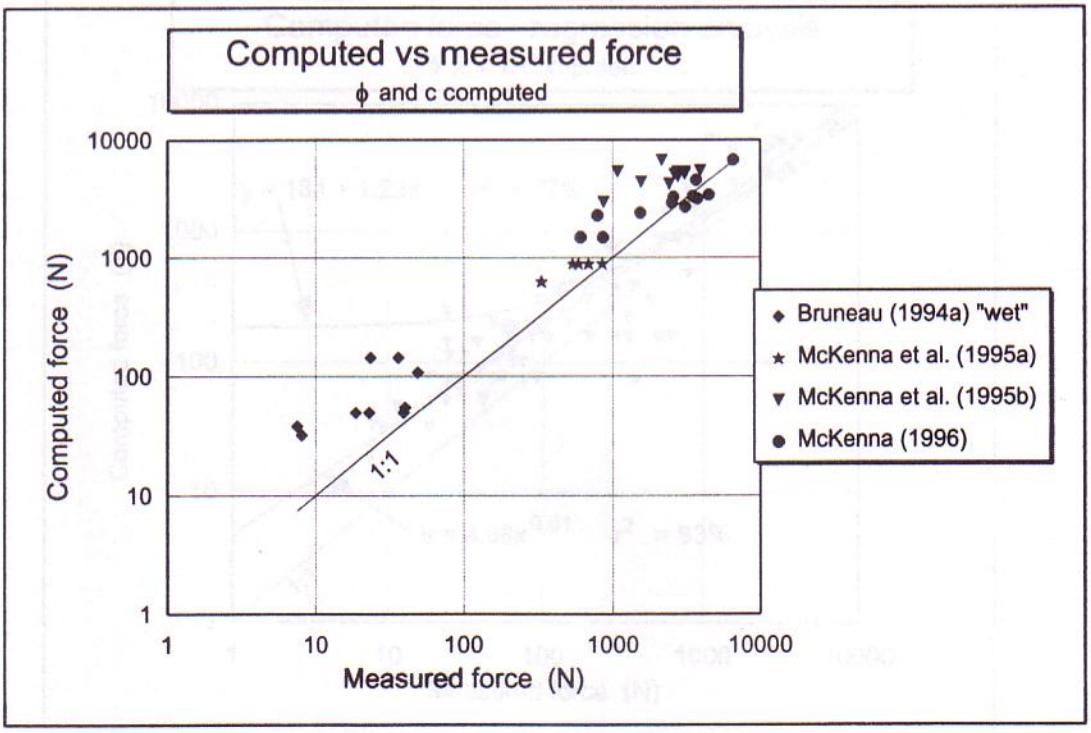

Figure 6.4 Force prediction study for "computed ϕ-c" - Chapter 3 data.

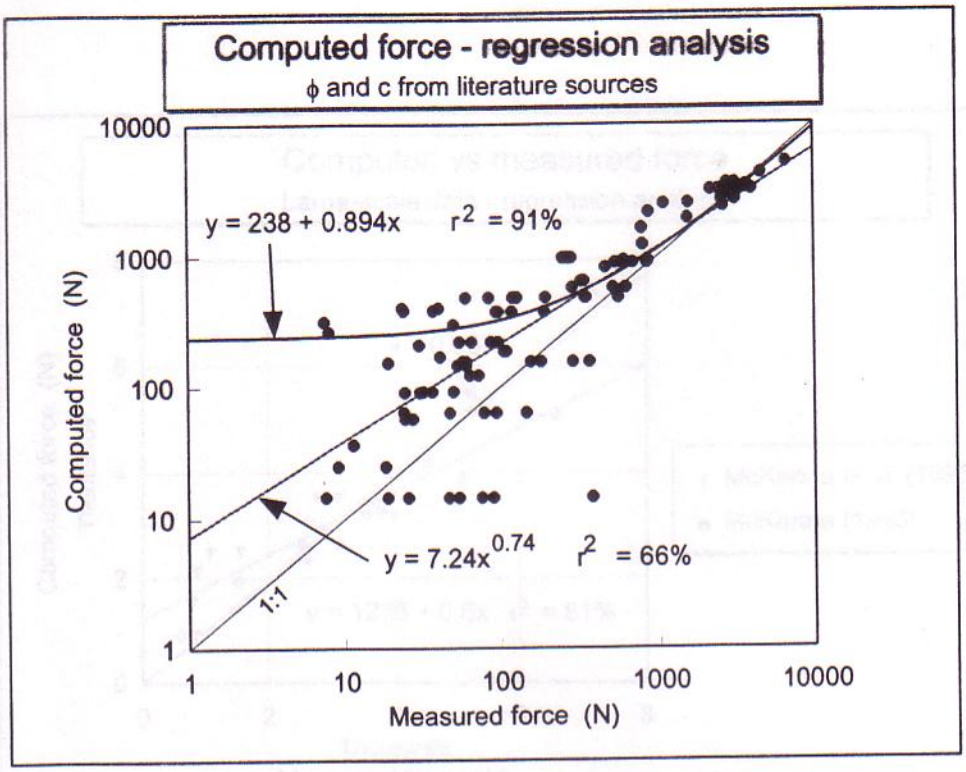

Figure 6.5 Force prediction study regression results "referenced ϕ-c" - base data set.

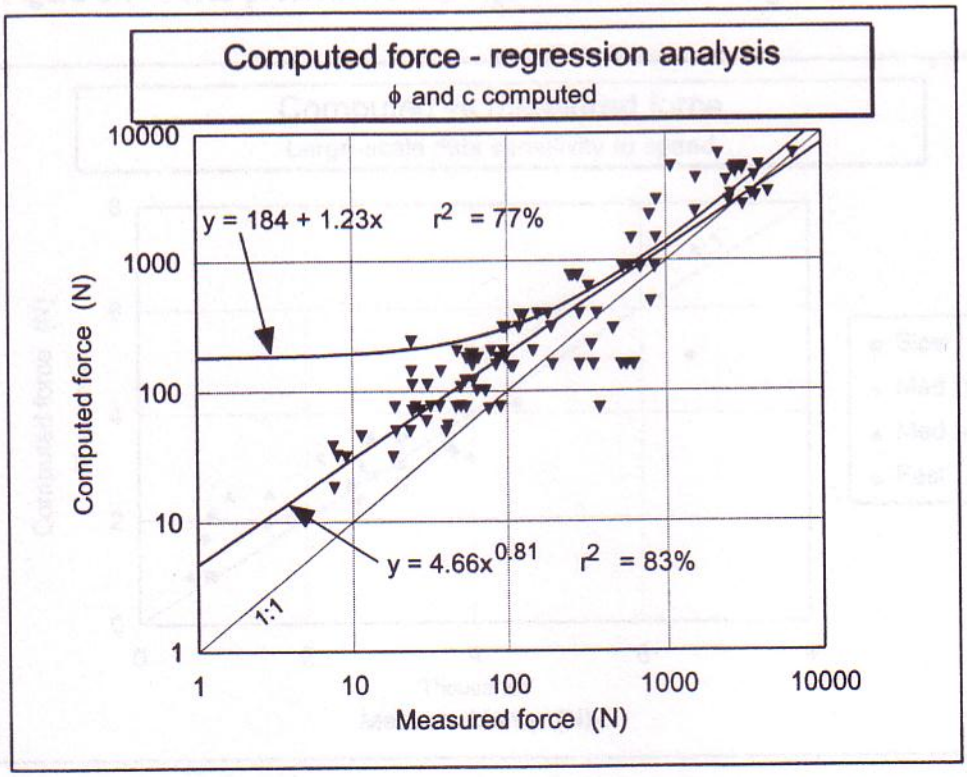

Figure 6.6 Force prediction study regression results "computed ϕ-c" - base data set.

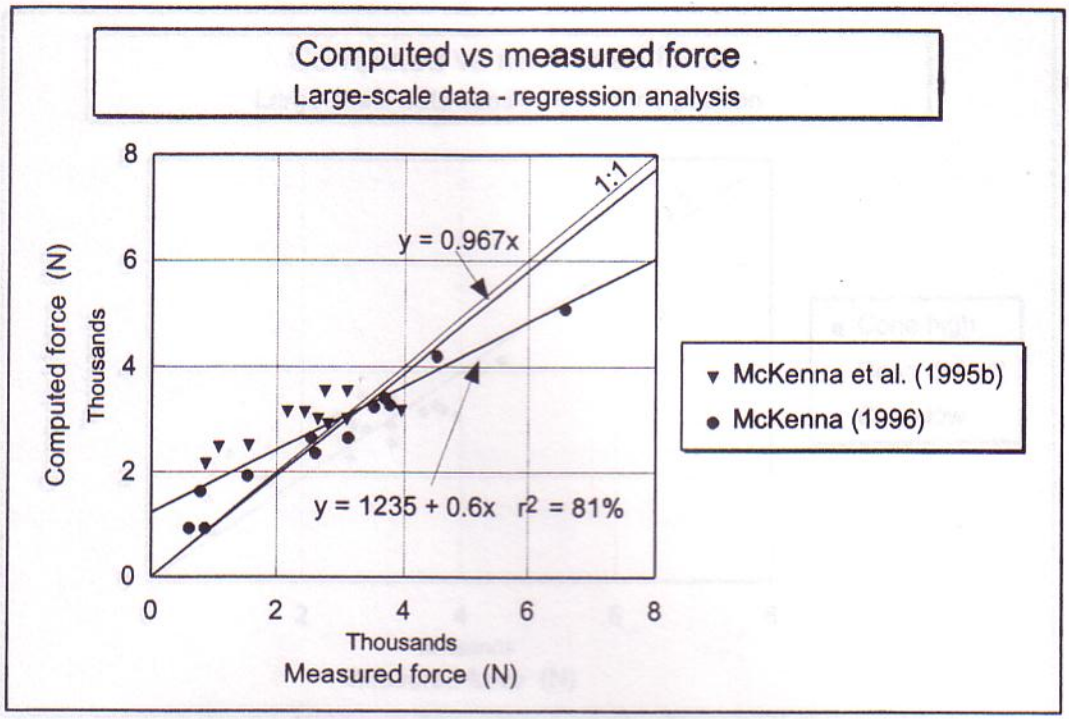

Figure 6.7 Force prediction study regression results - large-scale data sets.

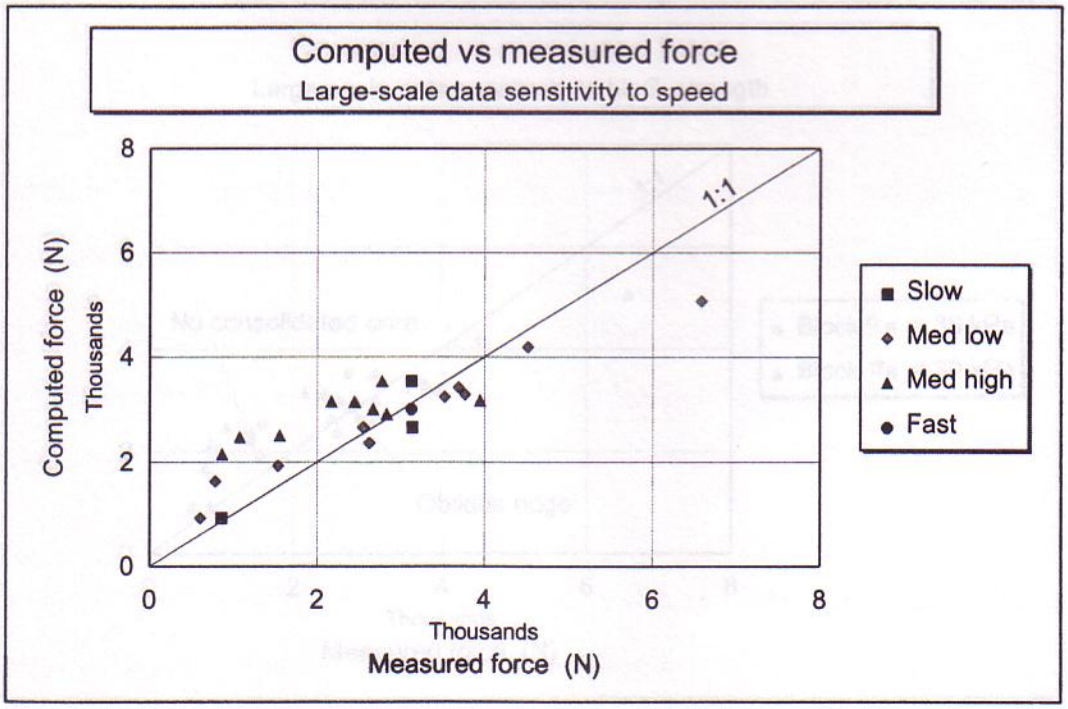

Figure 6.8 Force prediction study - large-scale data speed sensitivity.

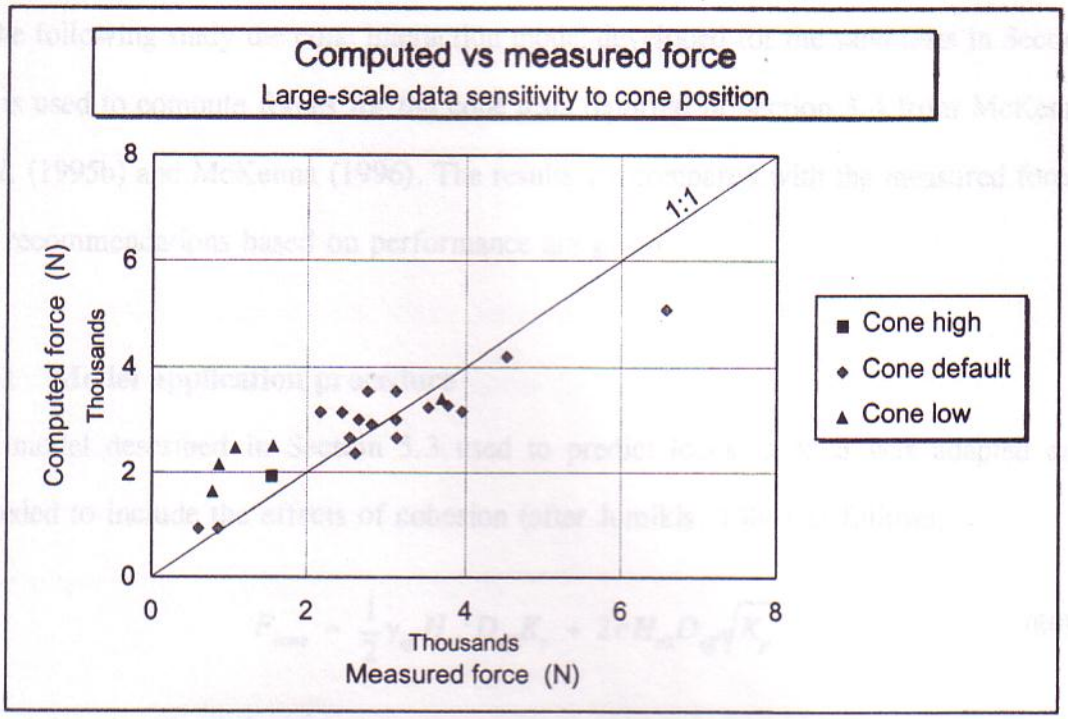

Figure 6.9 Force prediction study - large-scale data cone height sensitivity.

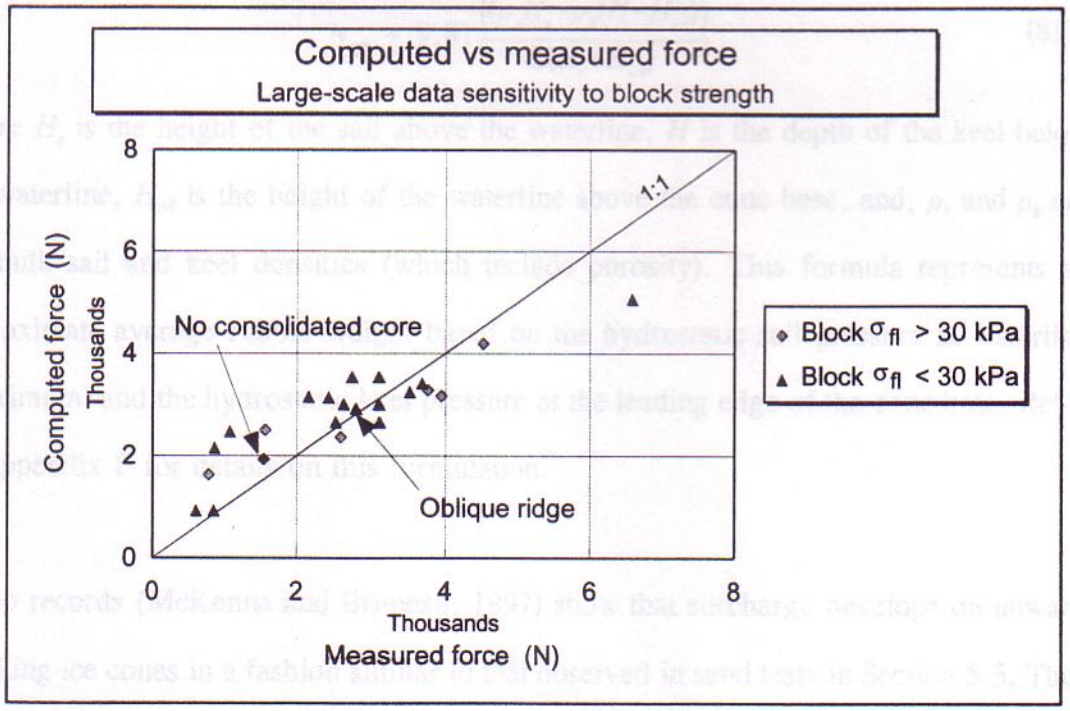

Figure 6.10 Force prediction study - large-scale data block strength sensitivity.

6.2 Conical structure interaction model

In the following study the cone interaction model developed for the sand tests in Section 5.3 is used to compute forces for the cone tests reported in Section 3.4 from McKenna *et al.* (1995b) and McKenna (1996). The results are compared with the measured forces and recommendations based on performance are given.

6.2.1 Model application procedure

The model described in Section 5.3 used to predict loads in sand was adapted and extended to include the effects of cohesion (after Jumikis, 1984) as follows:

$$F_{cone} = \frac{1}{2}\gamma_{eff} H_{t0}^{2} D_{eff} K_p + 2cH_{t0} D_{eff}\sqrt{K_p} \qquad (80)$$

In applying the above formula the effective ice rubble weight was estimated by

$$\gamma_{eff} = 9.81\frac{\left(\left(\rho_s H_s + \rho_k (H - H_{wl})\right)\right)}{2(H_s + H_{wl})} \qquad (81)$$

where H_s is the height of the sail above the waterline, H is the depth of the keel below the waterline, H_{wl} is the height of the waterline above the cone base, and, ρ_s and ρ_k are the bulk sail and keel densities (which include porosity). This formula represents an approximate average rubble weight based on the hydrostatic sail pressure at waterline (maximum) and the hydrostatic keel pressure at the leading edge of the cone base. Refer to Appendix F for details on this formulation.

Video records (McKenna and Bruneau, 1997) show that surcharge develops on upward breaking ice cones in a fashion similar to that observed in sand tests in Section 5.3. Thus the depth of the rubble H_{t0} acting on the cone can be approximated using the formula

derived in Section 5.3 which considers a non-linear build up of surcharge as follows:

$$H_{t0} = D_{av} * 0.59 \left[\frac{H_{se}}{D_{av}}\right]^{0.652} \left[\frac{\left[\frac{P_{en}}{D_{av}}\right]^2}{\left[\frac{P_{en}}{D_{av}}\right]^2 + \left[\frac{H_{se}}{D_{av}}\right]}\right]^{1.07} \quad (82)$$

where D_{av} is the average cone diameter between the waterline and the cone base. The sail height used, H_{se}, is the height of a "trapezoid-shaped" sail with a cross-sectional area matching the measured value. This adaptation is necessary to match the shape of the "sand keels" for which the expression for total depth above was derived. Thus H_{se} was determined from the following expression

$$A_{sail} = H_{se}\left[W - \frac{H_{se}}{\tan(32)}\right] \quad (83)$$

where A_{sail} is the sail cross-sectional area, W is the ridge width. The penetration into the ridge at peak load, P_{en}, is estimated from sand tests (Section 5.3) using the formula:

$$\frac{P_{en}}{D_{av}} = 0.57\left[\frac{W}{D_{av}}\right]^{0.723}\left[\frac{H_{se}}{D_{av}}\right]^{-0.0471} \quad (84)$$

The effective diameter the cone structure can be estimated by the formula

$$D_{eff} = D_{av}\left[1 + \frac{3H_{t0}}{2D_{av}}\right] \leq 2D_{av} \quad (85)$$

which was derived in Section 5.2 for vertical structures in sand.

The applicable form of the passive pressure coefficient K_p is that defined earlier in Section 5.3, Equation 68. The internal friction angle (and cohesion) used for the comparison were those reported in McKenna *et al.* (1996) where $\phi = 36°$ and $c = 438$ Pa. The cone slope was 45° and the ice-structure friction coefficient $\tan(\phi_1)$ was 0.14 from McKenna (1995b). The slope of the surcharge was estimated by the same model used in Section 5.3 for the sand tests and adapted as follow:

$$\delta = -atan\left[\frac{H_{t0}-H_{wl}}{r_o 4/\pi}\right] \tag{86}$$

This recognises that the overburden is humped in the shape of a cosine curve, for which this equation gives an average slope over the rupture distance, r_o, approximated from sand tests as:

$$r_o = D_{av}\left[0.535 + 2.06\left(\frac{H_{se}}{D_{av}}\right)\frac{\left(\frac{P_{en}}{D_{av}}\right)^2}{\left(\frac{P_{en}}{D_{av}}\right)^2 + \left(\frac{H_{se}}{D_{av}}\right)}\right] \tag{87}$$

6.2.2 Comparative study results

The preceding force computation procedure has been tested against measured force data. In Figure 6.11 predicted forces are plotted against measured forces for all cone longitudinal horizontal forces reported in Section 3.4 (after McKenna *et al.* 1995b and McKenna 1996). Forces are predicted reasonably well ($r^2 = 67\%$) though some scatter

exists which is pronounced for higher force data points. From Figure 6.12 and 6.13 one can see that the instances where the model significantly under-predicts are limited to tests where the cone was positioned low in the water and where flexural strength was high. To possibly explain these trends recall that with the cone positioned low in the water measured loads were lower than computed forces on the cylinder. The higher measured forces seen here may be compensating for this. The influence of the protruding cone base on rubble below it may explain these inconsistencies. An "effective depth" for the cone may be a consideration for future modelling. High flexural strength may influence the shear strength of rubble in the laboratory at IMD though this effect has not been recognised in the ϕ and c terms used in this force study.

Figure 6.14 shows that interaction speed does not influence the prediction of cone forces. It is important to note that inertia forces are not scaled linearly in the laboratory so that much higher speeds are required to examine this effect in practice. Nevertheless, speed effects which *may* have resulted from shear strength or surcharge formation dependencies are not evident in this study. The data points for both high and low speed tests are clustered around the 1:1 line.

The refrozen core flexural force component has not been removed from the measured forces in this study. This would tend to shift the points to the left in Figures 6.11 to 6.14. The force traces in McKenna (1995b) for the cone "X" force (the component considered here) appear, from video observation, to have a frequency component corresponding to flexural failure. Typically this component has an amplitude between 10 and 20% of the total transient ridge force. If the flexural resistance momentarily vanishes immediately after the collapse of a load cycle when the newly broken core ice becomes

indistinguishable from the accumulated rubble, then the flexural component is probably 10 to 20% of the forces shown. Figure 6.12 indicates the effect of rubble strength on the model performance and also shows the single data point which represents a test in which there is no refrozen core. The position of this point does not support the "core component" argument above, however, it is only one point and it also corresponds to the lowest cone position tested.

6.2.3 Conclusions

This study has successfully demonstrated the applicability of the sand cone model to ice rubble experiments. Sensitivities to cone position relative to the keel are noted. Speed had little influence on forces but higher block strength resulted in higher forces. The cone model presented has some intrinsic weaknesses which are difficult to overcome. For instance, the ice cone is not as steep as the sand cone and the formulas for surcharge height, rupture distance and penetration at peak are based on the sand cone. The effective diameter formula used for the cone was derived from vertical structure experiments in sand. Also the ice cone was not as high as the sand cone so that more rubble interacted with the cylindrical neck above the cone in ice than was the case in sand. Despite these limitations the procedure works well, is closed form, and does not require very much input data.

In the next chapter the application of the laboratory analytical models to full-scale is discussed. Considerations of speed effects resulting from fluid dynamics and global inertia are considered. A sensitivity trial calculation of full-scale forces on vertical structures is presented and a comparison of those results with full-scale data is attempted.

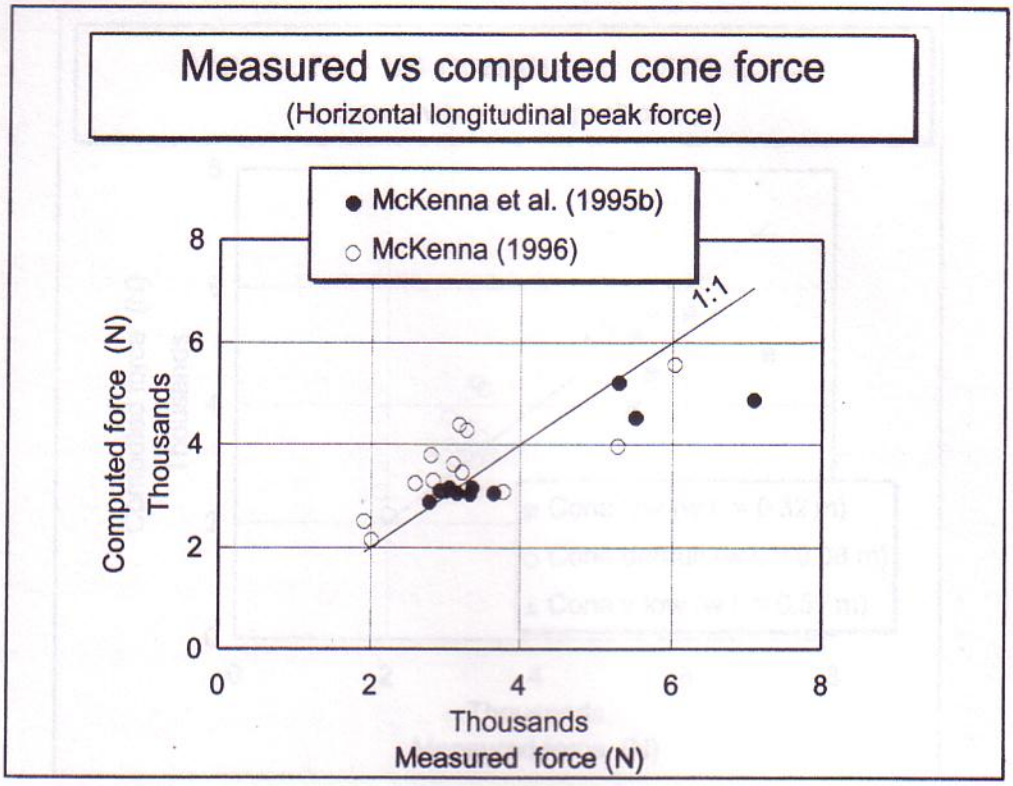

Figure 6.11 Cone force prediction study - by reference.

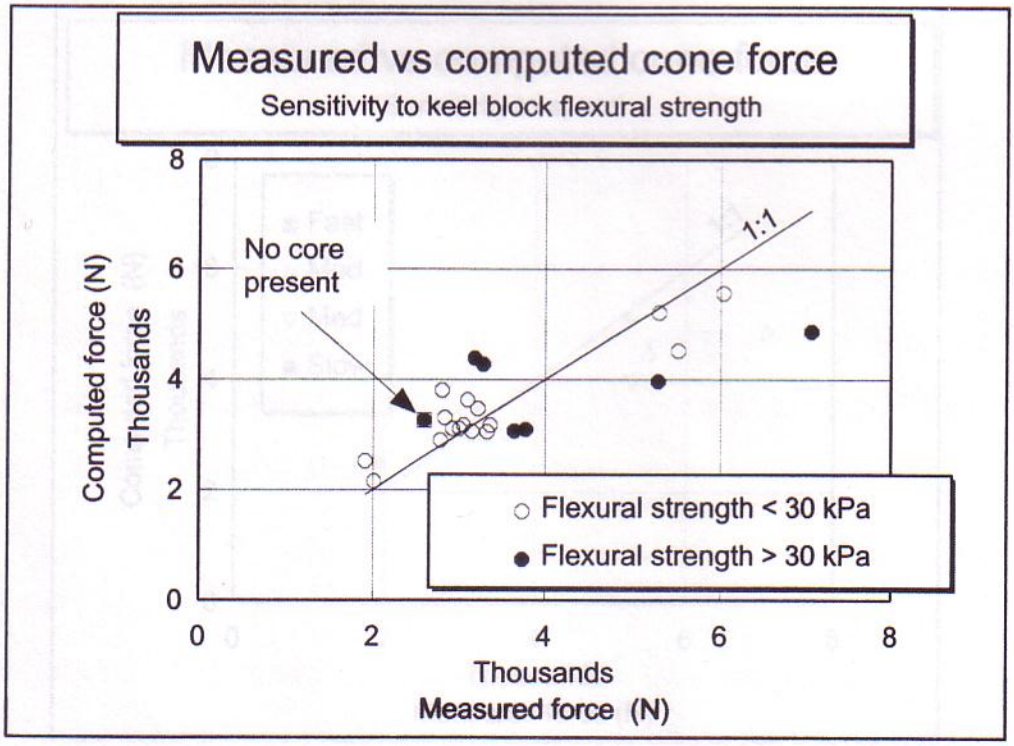

Figure 6.12 Cone force prediction study - block strength sensitivity.

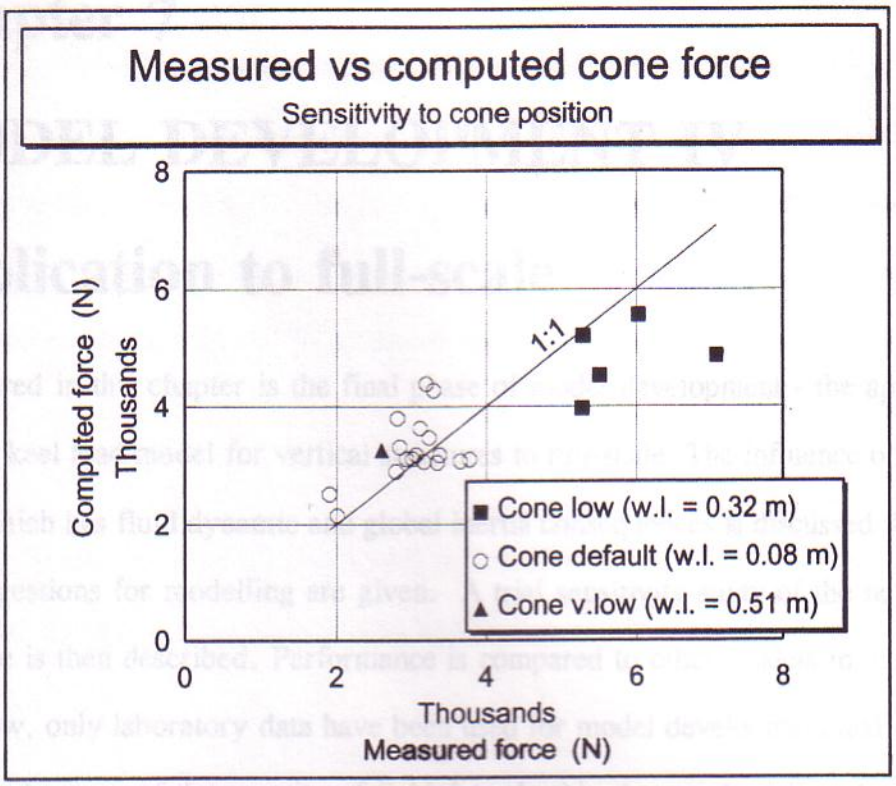

Figure 6.13 Cone force prediction study - cone position sensitivity.

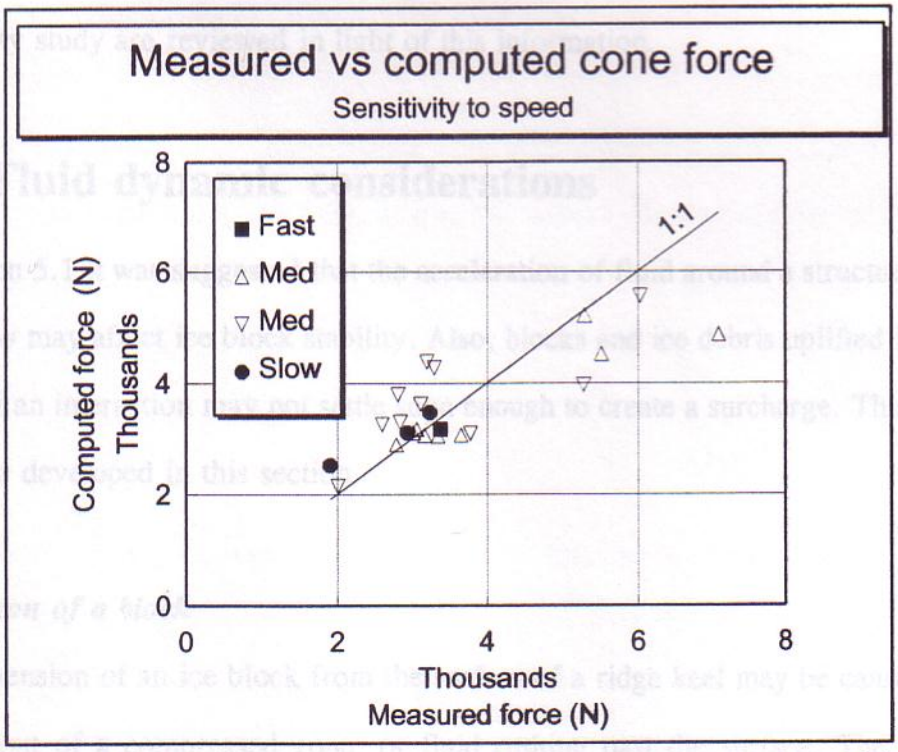

Figure 6.14 Cone force prediction study - interaction speed sensitivity.